Mon. Not. R. Astron. Soc. **307**, 584–594 (1999)

New constraints on a triaxial model of the Galaxy

Maartje Sevenster,[1,2]★ Prasenjit Saha,[1,3] David Valls-Gabaud[4,5] and Roger Fux[6]
[1]*Mt Stromlo and Siding Spring Observatories, Private Bag, Weston Creek PO, 2611 ACT Weston, Australia*
[2]*Sterrewacht Leiden, PO Box 9513, 2300 RA Leiden, the Netherlands*
[3]*Department of Physics, Keble Road, Oxford OX1 3RH*
[4]*UMR CNRS 7550, Observatoire de Strasbourg, 11 Rue de l'Université, 67000 Strasbourg, France*
[5]*Institute of Astronomy, Madingley Road, Cambridge CB3 0HA*
[6]*Geneva Observatory, Ch. des Maillettes 51, CH-1290 Sauverny, Switzerland*

Accepted 1999 March 11. Received 1999 March 11; in original form 1997 October 10

ABSTRACT

We determine the most likely values of the free parameters of an *N*-body model for the Galaxy developed by Fux via a discrete–discrete comparison with the positions on the sky and line-of-sight velocities of an unbiased, homogeneous sample of OH/IR stars. Via Monte Carlo simulation, we find the plausibility of the best-fitting models, as well as the errors on the determined values. The parameters that are constrained best by these projected data are the total mass of the model and the viewing angle of the central bar, although the distribution of the latter has multiple maxima. The other two free parameters, the size of the bar and the (azimuthal) velocity of the Sun, are less well-constrained. The best model has a viewing angle of $\sim 44°$, a semimajor axis of 2.5 kpc (corotation radius 4.5 kpc, pattern speed $46\,\mathrm{km\,s^{-1}\,kpc^{-1}}$), a bar mass of $1.7 \times 10^{10}\,\mathrm{M_{\odot}}$ and a tangential velocity of the local standard of rest of $171\,\mathrm{km\,s^{-1}}$. We argue that the lower values that are commonly found from stellar data for the viewing angle ($\sim 25°$) arise when too few coordinates are available, when the longitude range is too narrow or when low latitudes are excluded from the fit. The new constraints on the viewing angle of the Galactic bar from stellar line-of-sight velocities decrease further the ability of the distribution of the bar to account for the observed microlensing optical depth toward Baade's window: our model reproduces only half the observed value. The signal of triaxiality diminishes quickly with increasing latitude, fading within approximately 1 scaleheight ($\lesssim 3°$). This suggests that Baade's window is not a very appropriate region in which to sample bar properties.

Key words: stars: kinematics – Galaxy: structure.

1 INTRODUCTION

Evidence has accumulated over the last five years that there is a triaxial structure in the inner Galaxy (see Gerhard 1996 for a review). The study of the Galactic bar received a large stimulus when the *COBE* DIRBE data and derived models became available (Dwek et al. 1995). Earlier, star counts, gas dynamics and three-dimensional stellar kinematics had been analysed. Although most studies agree on the presence of a bar and roughly on its orientation, the exact viewing angle, size and shape remain a matter of debate. In this article we use for the first time a global set of stellar line-of-sight velocities in the Galactic plane to determine the values of these parameters, by comparing the set with a triaxial *N*-body model of the Galaxy (Fux 1997).

★ E-mail: msevenst@mso.anu.edu.au

N-body models are important for the study of the dynamics of the triaxial Galaxy, because they are self-consistent and have known formation and evolution history. This is in contrast to self-consistent Schwarzschild-type models (Schwarzschild 1979), for which we know only the present and the future. Schwarzschild-type models can be aimed directly at fitting observations. True *N*-body models can be 'steered' that way much less easily, and comparing them with observations is difficult. This holds especially for the Galaxy, where stellar kinematic data are always discrete and one is therefore faced with the problem of comparing two distributions of discrete data points. One could smooth and normalize the (projected) *N*-body model if it had sufficient particles and sample this probability distribution at the observed points. The result is the probability of the data given the model. One can also smooth the observations to obtain a velocity profile, as is often done with observations in Baade's window, and compare that with the corresponding, smoothed, *N*-body profile.

Statistical tests then yield the probability that the two distributions are the same.

We have the opportunity to use a new stellar–kinematic data set, homogeneous and unbiased, with highly accurate on-the-sky positions and line-of-sight velocities (Sevenster et al. 1997a,b, hereafter S97A, S97B). This data set (Australia Telescope Ohir Survey of the plane, hereafter AOSP) is particularly suited for constraining dynamical models for the Galaxy, not only because of its high accuracy but also because of the intrinsic properties of the stars. The AOSP sample consists of so-called OH/IR stars, observable throughout the Galaxy. These are evolved, intermediate-mass stars and their distribution, spatial as well as kinematic, traces closely the global Galactic potential (Frogel 1988; Habing 1993 and is relatively relaxed. OH/IR stars have circumstellar envelopes because of mass loss and the outflow velocity of those circumstellar envelopes can be obtained directly from the spectra. The outflow velocity is related to the stellar mass and thus to the age of the star, in a statistical sense (van der Veen 1989; see Sevenster 1997). This allows, for example, determination of the changes in the dynamical distribution with time.

The average surface density of the sample is of the order of one star per square degree. This means that two neighbouring stars cannot be assumed to sample the same velocity profile, which is implicitly required to smooth the data. Also, it is not necessary to smooth the model completely, because we want to determine the probability of the model given the data, rather than the other way round, or the probability that model and data have the same distribution. We use a method to scale an *N*-body model (Fux 1997) to match the data, via an implementation of a direct discrete–discrete comparison (Saha 1998). The model was chosen from a range of *N*-body models because it reproduces best the combination of the *COBE* DIRBE surface-density map [in the *K* band (2.2 μm)] and other observations (e.g. the local dispersions and density; Fux 1997). It is therefore most representative for the AOSP sample, because this comes from exactly the same intermediate-mass, evolved stellar population that dominates the near infrared surface density observed by *COBE*.

In Section 2 we describe briefly the general method for the Galaxy model–data comparison, in Section 3 we describe the detailed implementation for the given data and model we use. The results are presented and discussed in Sections 4 and 5. In Section 6 we calculate the implications for gravitational microlensing toward the Galactic bulge, and we finish with our conclusions in Section 7.

2 THE METHOD

2.1 Determining the best fit

To compare the six-dimensional *N*-body model (Cartesian coordinates x, y, z, u, v, w) and the three-dimensional data (Galactic longitude ℓ and latitude b, and line-of-sight velocity V), the model is projected according to

$$x' = x\cos\phi + y\sin\phi, \qquad y' = y\cos\phi - x\sin\phi + \mathrm{R}_\odot,$$

$$u' = u\cos\phi + v\sin\phi, \qquad v' = v\cos\phi - u\sin\phi,$$

$$\ell = \arctan\left(\frac{-x'}{y'}\right), \qquad b = \arctan\left(\frac{z}{\sqrt{[x']^2 + [y']^2}}\right),$$

$$V = f_V\left\{\frac{x'u' + y'v' + wz}{\sqrt{[x']^2 + [y']^2 + z^2}}\right\} - \mathrm{V}_\odot \sin\ell\cos b. \tag{1}$$

The four scaling parameters ϕ, $\mathrm{R}_\odot$, f_V, $\mathrm{V}_\odot$ are the free parameters of the model. The viewing angle ϕ is the orientation of the bar with respect to the line of sight to the Galactic Centre (if $\phi = 0°$ the bar points toward the Sun). $\mathrm{R}_\odot$ enters equation (1) as if it were the distance of the Sun from the Galactic Centre, but it determines the size of the bar (ℓ, b become smaller with larger $\mathrm{R}_\odot$). If in the initial model the semimajor axis is a, then in the scaled model it is $(a \times 8\,\mathrm{kpc}/\mathrm{R}_\odot)$. This is the consequence of having only (ℓ, b, V) to fit; if we had more coordinates there would be an extra free parameter f_R (the true size scale) and $\mathrm{R}_\odot$ would be the true distance to the Galactic Centre. In equation (1) this parameter f_R is hidden, as it enters the numerator as well as the denominator for all three coordinates and thus is of no consequence. The velocity factor f_V determines the total mass, $M_\mathrm{p} \propto f_V^2\ (8\,\mathrm{kpc}/\mathrm{R}_\odot)$ (maintaining virial equilibrium). $\mathrm{V}_\odot$ is the azimuthal velocity of the local standard of rest (LSR). The four free parameters are all weakly correlated, as is clear from the fact that we have only three quantities to fit. In equation (1) we see immediately that the spatial distribution of the data places no constraints on f_V and $\mathrm{V}_\odot$. The line-of-sight velocities do constrain $\mathrm{R}_\odot$, which enters the coordinate-transformation term as well as the solar motion correction term in the expression for *V*. The viewing angle ϕ plays a prominent role in all terms of equation (1).

We determine the values of the free parameters that optimize the model–data fit with a so-called genetic programming method (Charbonneau 1995). We divide the three-dimensional data space into $B \equiv N_\ell N_b N_V$ boxes and determine the number of model and data particles in each box, i, m_i and o_i, respectively. The joint probability W that the data (in total O particles) and the model (M particles), projected on the data space, arise from the same underlying distribution function, is given by the following formula (Saha 1998):

$$W = C\prod_{i=1}^{B}\frac{(m_i + o_i)!}{m_i! o_i!}, \qquad C = \frac{M!O!(B-1)!}{(M+O+B-1)!},$$

$$o_i, m_i = o_i, m_i(\phi, \mathrm{R}_\odot, \mathrm{V}_\odot, f_V). \tag{2}$$

Note that this equation is symmetric in the model and data terms. W is robust against outliers in the data (or in the model if $M<O$, which is unlikely ever to be the case) and also against unphysical solutions, such as putting all M model particles in the box with highest o_i (Saha 1998).

If $m_i = 0$ or $o_i = 0$, no contribution to the likelihood W is made; the term within the product in equation (2) equals 1. Preferably, $B < M$ and $B < O$ so that we have as few boxes as possible without information content. On the other hand, we want to prevent any smoothing of the data, so that $o_i \lesssim 1$ for all i and $B > O$. In other words, $B \sim O$, which results in $B < M$ as $M \gg O$. A fundamental constraint on the box size comes from the demand that, within a box, the distribution function that M and O derive from is constant. This constraint is much harder to quantify in practice, because we do not know the distribution function. In general it is also in conflict with the first constraint. If we make the boxes so small that the distribution function is truly constant within each of them, not all will contain at least one star. A proper balance has to be found between the two constraints. From tests we find that results are robust over a large range of B: $2O < B < 8O$.

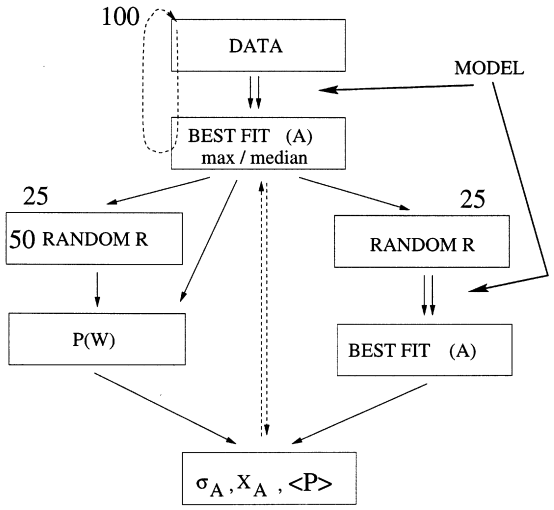

Figure 1. Schematic view of the procedure to determine the W distribution (left branch) and the intrinsic error in the free parameters A (right branch). The double arrows indicate the steps that involve optimizing (of W). First, the maximum of $W(\phi, \mathrm{R}_\odot, \mathrm{V}_\odot, f_V)$ (equation 2) is determined with a genetic algorithm for 100 different subsets of the model. From the results, best-fitting A values are determined (see Section 2.1). From the model, scaled with parameter values A, 50 random samples of O particles are drawn and the value of W for each of these 'data sets' given the scaled model is calculated. The whole left branch is executed 25 times, yielding the plausibility $\langle P \rangle$ (see Section 2.2). On the other branch, 25 random samples of O particles are drawn from the scaled model. For each of those, again $W(\phi, \mathrm{R}_\odot, \mathrm{V}_\odot, f_V)$ is optimized, i.e. using the initial model. The resulting distributions in $\phi, \mathrm{R}_\odot, \mathrm{V}_\odot, f_V$ yield the errors σ and the biases X in the fitted values.

For both larger and smaller B/O the plausibilities start going to zero, although the best-fitting values remain constant for smaller B/O. Judging by the values, biases and plausibilities of our tests, $B/O \sim 4$ is optimal.

In principle all model particles could be used for optimizing equation (2), but in practice we use random subsets with $M = 16\,384$, saving calculation time without losing precision. We carry out the optimization for 100 such subsets to obtain a number distribution of best-fitting values for each parameter (see Fig. 1) We then determine the medians of these distributions, or all local maxima if there are more than one (only ϕ, as will be clear later), thus finding one or more best fits $(\phi, \mathrm{R}_\odot, \mathrm{V}_\odot, f_V)$.

2.2 Determining the plausibility

Having found a *best* fit to the data, we want to know whether it is also a *good* fit, within the limits of the model. Via Monte Carlo simulation (e.g. Press et al. 1986) we determine the 'intrinsic' W distribution for the best-fitting model. Sets of O model particles are randomly selected from the (entire) best-fitting model and the corresponding value of W is calculated. The resulting distribution thus gives the W values for the case in which we know that the model and the 'data' are the same. We then determine the percentage $P(W)$ of these values that is lower than the W of the real data. A high value of $P(W)$ means that the result is significant; the fit is as good as can be expected for that particular model. We carry out this loop (the left branch in Fig. 1) 25 times, with 50 different random subsets each time, to obtain $\langle P \rangle$. We will call $\langle P \rangle$ the plausibility of the fit. Roughly, models with $\langle P \rangle < 10$ per cent are not acceptable, models with $\langle P \rangle > 50$ per cent are optimal.

2.3 Determining the errors

To quantify the errors that are connected with the determination of a best-fitting model, we again draw random samples of O particles from the (entire) best-fitting model and find the best fit for these fake data sets. The mean values for each of the free parameters from these fits, and the dispersion in the values, show the intrinsic accuracy of the fitting procedure. For each quantity A, we thus find the 1σ error σ_A and the difference between the best-fitting value and the Monte Carlo mean, in terms of the 1σ error, the bias $X_A \equiv (A_{\mathrm{mean}} - A_{\mathrm{fit}})/\sigma_A$. In practice, we use 25 independent samples, created in such a way that $O \cap M = \emptyset$.

3 IMPLEMENTATION

3.1 Model and data particles

The N-body model we use is the model 'm08t3200' (at 3.2 Gyr in the simulation) developed by Fux (1997). It contains a bar that formed spontaneously (without imposed triaxial potential) from an axisymmetric distribution of stars, in a disc and a spheroid, plus a dark halo. The stellar part consists of 100 000 particles of $6.57 \times 10^5\,\mathrm{M}_\odot$. Corotation is at 5.4 kpc (determined from the moments of inertia) and the semimajor axis of the bar is 3 kpc (out to the start of spiral arms, around the inner ultraharmonic resonance) in the initial model. The circular velocity, at the radial range in which it is constant, is $218\,\mathrm{km\,s^{-1}}$, so the pattern speed of the bar is of the order of $40\,\mathrm{km\,s^{-1}\,kpc^{-1}}$. The in-plane axis ratio of the model bar is approximately 0.5. Symmetry with respect to the plane was imposed during the simulation. The ratio of the corotation radius to the semimajor axis is 1.8, which, together with an exponential density profile, makes this a late-type bar (Elmegreen 1996; Noguchi 1996).

The AOSP data set consists of 507 OH/IR stars (Section 1) with measured on-the-sky positions, accurate to 0.5 arcsec, and line-of-sight velocities, accurate to $1\,\mathrm{km\,s^{-1}}$. The observational errors are effectively zero in this analysis and will be neglected in the rest of this article. The properties of the stars in the AOSP sample (Section 1) allow us to gain more information from this modelling than just the best fit to the full data set. The outflow velocity of the circumstellar envelope, of the order of $15\,\mathrm{km\,s^{-1}}$, is roughly proportional to luminosity (van der Veen 1989), mass and age (because these are all effectively the same parameter, given a certain stellar evolution phase). The relation should be applied in a statistical sense. Stars with higher outflow velocities can hence be detected out to larger distances ($\gtrsim$12 kpc), on average, than those with lower outflow velocities ($\lesssim$10 kpc; Sevenster 1997), provided they are observed with the same flux-density cut-off (S97A, S97B). The spectra of some of the stars (<20 per cent) show only one of the usual two peaks, thus not allowing for a determination of the outflow velocity and an accurate line-of-sight velocity (S97A, S97B). For these stars, as a group, the velocity accuracy is of the order of the average outflow velocity, $15\,\mathrm{km\,s^{-1}}$. We applied the method to the total AOSP sample as well as to subsamples, to see how their different properties influence the fit (Section 3.3). The line-of-sight velocities of the stars are given with respect to the local standard of rest (LSR, see S97A).

Table 1. Windows for the runs ($M = 16\,384$).

Name	ℓ °	b °	V km s^{-1}	N_ℓ	N_b	N_V	O	B	description
bd	−45.5, 10.5	−3.25, 3.25	−300, 300	20	6	15	500	1800	all
b	−10.5, 10.5	−3.25, 3.25	−300, 300	10	6	15	303	900	bulge
bdd	−45.5, 10.5	−3.25, 3.25	−300, 300	20	6	10	410	1200	double-peaked
bdh	−45.5, 10.5	−3.25, 3.25	−300, 300	20	6	10	250	1200	high Δv
bdl(l)	−45.5, 10.5	−3.25, 3.25	−300, 300	20	6	10	250	1200	low Δv
fix*	−45.5, 10.5	−3.25, 3.25	−300, 300	20	6	15	500	1800	ϕ/R$_\odot$/V$_\odot$/f_V fixed
vel	−45.5, 10.5	−3.25, 3.25	−300, 300	20	4	20	500	1600	large N_V
mor	−45.5, 10.5	−3.25, 3.25	−300, 300	40	4	10	500	1600	large N_ℓ
morx	−45.5, 10.5	−3.25, 3.25	−300, 300	100	15	1	500	1500	$N_V = 1$
ptl	−25., 25.	−5., 5.	−250, 250	20	5	8	225	800	*IRAS* based

Throughout this article, we will use V$_\odot$ and 'solar motion' to indicate the azimuthal motion of the LSR.

3.2 The final runs

The outflow velocity of OH/IR stars correlates, as mentioned above, with average distance. We used that property by running the fitting program with various subsets of the data. In Table 1 the windows on the sky, the number of boxes in each coordinate, the number of stars O and the total number of boxes B that we used in the various runs are given. For all runs, $M = 16\,384$ so that the fits do not depend on the number of model particles within the window.

As mentioned in Section 2.1, optimally $B/O \sim 4$. The 'standard' run **bd** uses the total AOSP sample and the total region on the sky. Setting $(N_\ell, N_b, N_V) = (20, 6, 15)$ was found to be optimal in tests for this run. They correspond to bin sizes of 2.°75, 1.°1 and 40 km s^{-1}. For the other runs, we try to stick to those values of B/O and the bin sizes as closely as possible, given the characteristics of each individual run.

In run **b**, we use the largest possible longitude range symmetric about the Galactic Centre. In run **bdd**, we use only sources with double-peaked spectra, because they have the best-defined line-of-sight velocities, with, for this application, negligible errors (1 km s^{-1}; S97A, S97B).

In run **bdl** we use only sources with outflow velocities between 1 and 15 km s^{-1} and in run **bdh** only those with outflow velocities larger than 13 km s^{-1}. The ranges in outflow velocities overlap slightly in order to retain sufficient stars for the comparison.

The **bdh** contains stars at large distances (Section 3.1) and the fit for this run will be sensitive to the full morphology of the bar. For run **bdl**, the data particles and model particles probably do not trace the same distances; the subsample is complete out to $\lesssim$10 kpc (Section 3.1). We have therefore run **bdll** with a distance window (0–10 kpc) for the model.

To assess the degree to which the fit is determined by the stellar velocities or by their positions, we ran the program with increased velocity resolution (**vel**) and spatial resolution (**mor**), respectively. Those two runs have the same B and O to facilitate comparison. We also 'switched off' the kinematics completely (**morx**), as an extreme test, keeping in mind that $N_V = 1$ does not satisfy the demands on the box sizes. Finally, to judge better the suitability of the AOSP sample for constraining the free parameters of the N-body model, in **ptl** we used a different sample of OH/IR stars (te Lintel Hekkert et al. 1991). This sample is incomplete in a number of ways. First, it is an *IRAS*-selected sample, which means it is incomplete at very low latitudes, where confusion has limited the number of point sources detected by the *IRAS* satellite. Secondly, the velocity coverage changes with longitude. Thirdly, the infrared selection (see te Lintel Hekkert et al. 1991) introduces an inhomogeneous distance sampling that is difficult to quantify. The reason for using this sample nevertheless, or actually because of all this, will become clear.

In **fixf** we fix all parameters, except ϕ, at the values found by Fux (1997) for the model m08t3200; the value used for V$_\odot$ is that of the local circular velocity in his best-fitting model. Furthermore, we fix ϕ in **fix1** at 25°, in **fix2** at 45° and in in **fix3** at 65°, all three maxima in the distributions of best-fitting values of ϕ in various runs.

3.3 The search ranges

In preliminary tests, we found that the optimal search ranges are 0°–90° for ϕ, 6–10 kpc for R$_\odot$, 160–230 km s^{-1} for V$_\odot$ and 0.25–2.25 for M_p. As scaling the total mass means scaling the potential, and hence the velocities squared, in practice we determine this parameter by scaling a velocity factor f_V between 0.5 and 1.5, $M_\mathrm{p} \propto f_\mathrm{V}^2$. The only exception is run **morx**, where we use 0.3–3.0 for f_V. For the observable quantities, these ranges span the likely real values amply.

4 RESULTS

Figs. 2–5 show the results of the 100 W optimizations (see Fig. 1) for some of the runs. The values of the free parameters are found to be virtually uncorrelated, so that we can determine the maxima or medians of these distributions for each parameter separately to obtain the best-fitting models (ϕ, R$_\odot$, V$_\odot$, f_V). Clearly, the distributions of R$_\odot$ and V$_\odot$ do not have well-defined maxima (inside the search range). We use the median value for those parameters, as well as for f_V. The latter's distribution has the best-defined maximum of all four parameters (except in **morx**), but owing to its symmetric and smooth distribution the maximum is the same as the median value in all cases. We find several clear local maxima only for ϕ and determine these from the derivatives of the cumulative number distributions (i.e. the unbinned actual number distributions; see the dashed curves in Figs. 2–5).

In Table 2, we give the sets of best-fitting values for each of the runs described, along with the plausibility $\langle P \rangle$ of this best fit and the spread in the plausibility σ_P. For each of the parameters, we also give the 1σ error, σ_A, and the difference between the best-fitting value and the bias X_A, determined as described in Section 2. It should be noted that for best-fitting values at an upper or lower boundary of a search range, X_A is necessarily large, negative or

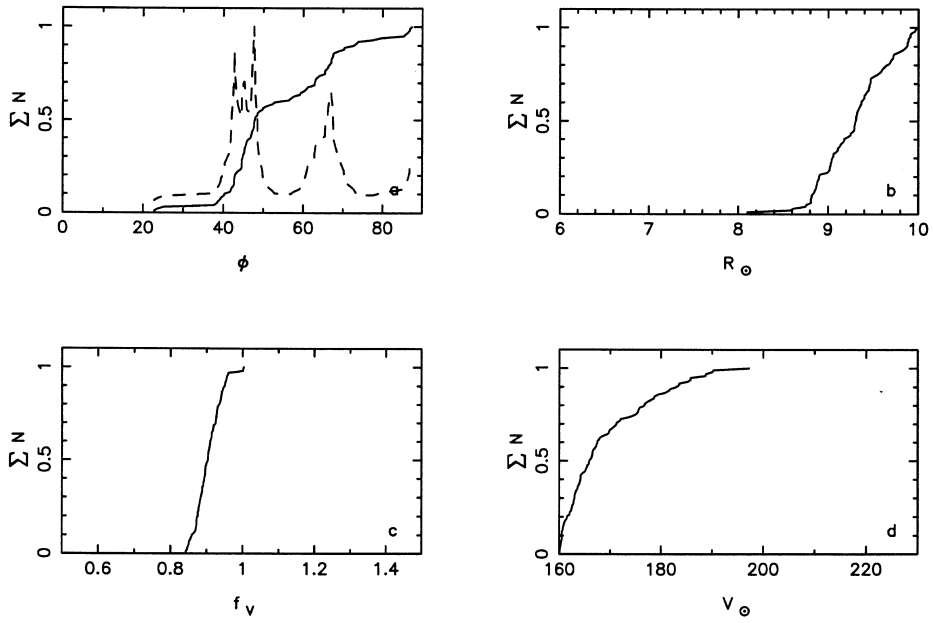

Figure 2. The cumulative number distributions from the 100 best-fitting values for the four free parameters from run **bdd**. For ϕ (panel a), the dashed curve gives the (arbitrarily normalized) derivative of the cumulative number distribution and hence shows the (unbinned) actual number distribution.

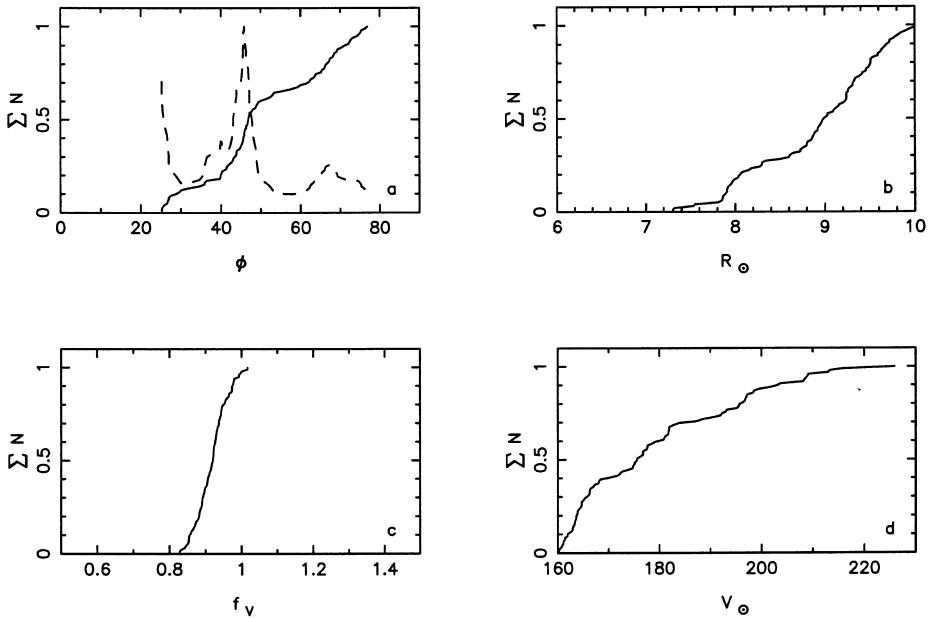

Figure 3. As Fig. 2, for run **bdl**.

positive, respectively. In run **morx** without the kinematics, the parameters $V_\odot$ and f_V (in italics) are not constrained at all.

In general, it is clear that $R_\odot$ and $V_\odot$ are not optimally constrained by our method and/or data. Their best-fitting distributions do not show clearly isolated maxima and from Table 2 we see that these parameters have average biases of ~0.5, as opposed to ~0.2 for ϕ and f_V. In terms of the ratio of σ_A to the corresponding search range, f_V is very well confined with σ_f on average 5 per cent of the search range. For the three other parameters this ratio is 20–25 per cent. There is good agreement to within $\sim 1\sigma$ between the various models (except **b, bdll, morx** and **ptl**, this will be discussed later) on the values of the parameters $R_\odot$ (8.9–9.6), $V_\odot$ (164–179) and f_V (0.90–0.95). For ϕ the situation is considerably different. Interestingly, despite the fact that the best-fitting distribution of ϕ mostly has several maxima, the subsequent Monte Carlo analysis of each of the solutions shows that some are remarkably well confined. In Fig. 6 we show the histograms of the values for ϕ in Table 2 as well as of all the values for ϕ occurring in the 100 optimizations for the six **bd*** runs. The three peaks around 25°, 45° and 65° obviously instigated the runs **fix1–3**. We disregard the fourth peak at 85° as this really indicates an axisymmetric solution. For $\phi = 90°$ (side-on), the surface-density profile is completely symmetric.

In principle, run **bd**, using the largest number of data points and the largest longitude window, should give the best results. Of its three solutions, the 44° fit coincides most closely with fits from

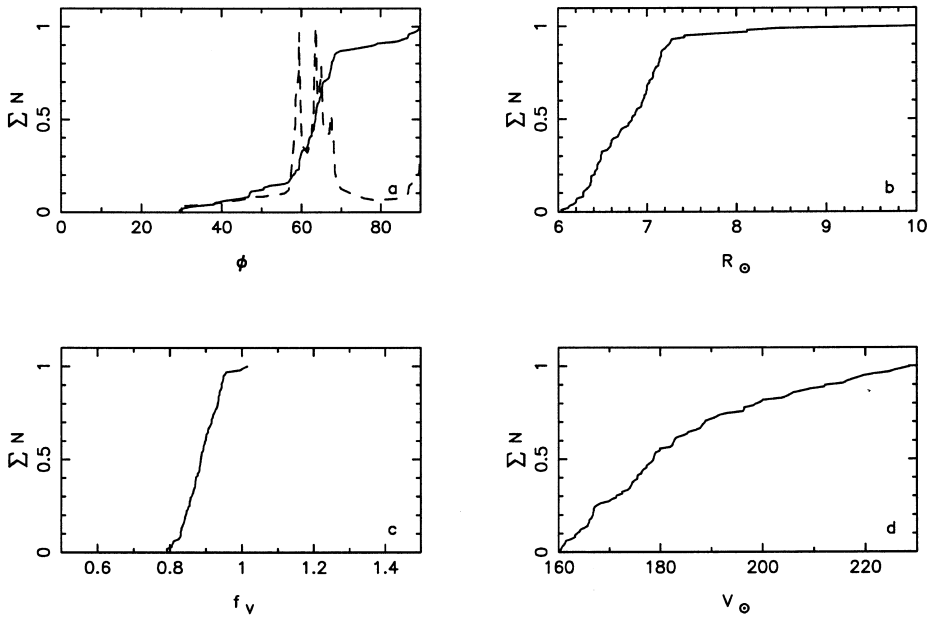

Figure 4. As Fig. 2, for run **bdll**.

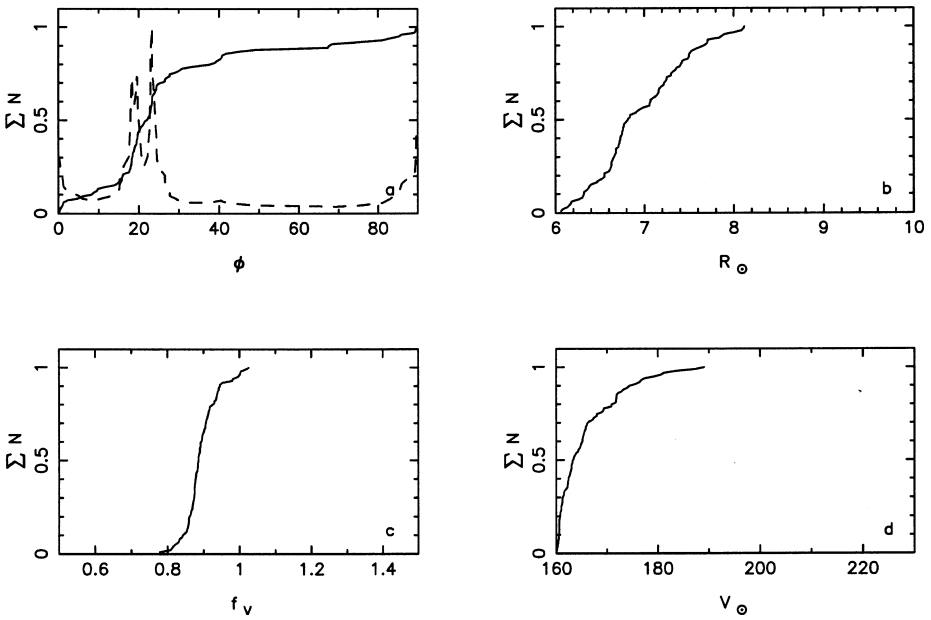

Figure 5. As Fig. 2, for run **ptl**.

several other runs (Fig. 6). Most notably, the runs with increased velocity accuracy, either from the data (**bdd**) or from the method (**vel**), have a solution for similar ϕ with very small bias in ϕ. Also **bdh**, which samples completely all distances throughout the bar, has a fit with $\phi = 45°$. These four $\phi \sim 44°$ runs give similar values for $R_\odot$ and $V_\odot$, and reasonable agreement for f_V. Moreover, the **bdh** $\phi = 45°$ fit has very high plausibility, as has **fix2** with respect to **fix1,3**. The $\phi = 44°$ result for **bd** (to be called **bd1**) therefore gives the best scaling parameters for Fux's *N*-body model.

4.1 The degeneracy in ϕ

Obviously, there are other values of ϕ that give equally reasonable fits (judging by the errors, biases and plausibilities). In the lower panel of Fig. 6, we see that ϕ even follows an intrinsically quadrumodal distribution! It was shown by Zhao (1997b) that, from surface density only, the viewing angle cannot be determined uniquely. Different density models for the bar can give exactly the same projected densities with different viewing angles. It is expected, however, that no such degeneracy would exist when optimizing a given spatial density model, or when including global kinematics constraining self-consistent model dynamics. The fact that we still find a degeneracy is probably at least partly dictated by the limited extent of our longitude window at positive longitudes. 'Asymmetry profiles' (positive-to-negative longitude ratios of surface density or mean velocity etc.) are crucial in constraining ϕ and these profiles are cut short. In the next paragraph we discuss what influence this may have.

Table 2. Best-fitting parameter values (local maxima for ϕ, medians for $R_\odot$, M_p, $V_\odot$) and plausibilities.

Name	ϕ °	σ_ϕ °	X_ϕ	$R_\odot$ kpc	σ_R kpc	X_R	f_V	σ_f	X_f	$V_\odot$ km s^{-1}	σ_V km s^{-1}	X_V	$\langle P \rangle$ %	σ_P %	description
bd(1)	**44**	15	−0.35	**9.5**	0.5	−0.15	**0.95**	0.04	−0.20	**171**	16	0.6	15	7	all
	59	20	−0.02	9.5	0.4	−0.03	0.95	0.04	−0.21	171	18	0.4	28	10	
	71	16	0.08	9.5	0.5	−0.28	0.95	0.04	−0.11	171	16	0.5	15	8	
b	55	25	−0.58	9.7	1.3	−0.79	0.99	0.08	−1.00	212	18	−0.9	52	12	bulge
	60	19	−0.25	9.7	0.5	−0.90	0.99	0.09	−0.03	212	**21**	−0.7	60	13	
	68	18	−0.00	9.7	0.6	−0.79	0.99	0.06	−0.83	212	24	−1.0	56	11	
bdd	43	21	−0.06	9.3	0.7	−0.34	0.90	0.03	−0.03	166	13	0.5	54	10	double-peaked
	48	19	−0.54	9.3	0.6	−0.08	0.90	0.05	−0.02	166	**15**	0.7	57	10	
	67	13	0.33	9.3	0.6	0.16	0.90	0.04	0.19	166	16	0.8	57	10	
bdh	45	20	−0.43	9.6	0.4	−0.41	0.90	0.06	−0.04	164	7	1.1	71	7	high Δv
	61	24	−0.36	9.6	0.5	−0.59	0.90	0.06	0.15	164	15	0.8	66	9	
	83	14	−1.11	9.6	0.5	−0.49	0.90	0.06	0.27	164	15	0.7	57	9	
bdl	25	18	−0.07	9.0	0.7	0.09	0.92	0.05	0.15	176	16	0.2	17	8	low Δv
	46	22	−0.16	9.0	0.7	0.28	0.92	0.08	0.09	176	22	0.4	52	**8**	
	67	14	−0.22	9.0	0.8	−0.11	0.92	0.07	−0.33	176	17	0.1	43	10	
bdll	59	19	0.25	6.8	0.7	0.66	0.89	0.06	−0.39	179	21	0.2	30	9	low Δv, $d_{\rm lim} = 10$
	64	15	−0.13	6.8	0.8	0.48	0.89	0.06	−0.10	179	17	0.8	34	9	
vel	44	18	−0.09	9.5	0.6	−0.36	0.94	0.06	0.10	169	15	0.5	10	5	large N_V
	56	21	−0.24	9.5	0.6	−0.15	0.94	0.05	−0.53	169	14	0.4	7	5	
	64	21	−0.30	9.5	0.6	−0.48	0.94	0.03	−0.53	169	14	0.4	13	8	
mor	41	16	−0.26	8.9	0.7	0.44	0.92	0.05	0.03	166	14	0.8	18	7	large N_ℓ
	54	16	−0.11	8.9	0.6	0.46	0.92	0.04	0.05	166	18	0.7	25	10	
	58	20	0.01	8.9	0.6	0.36	0.92	0.04	−0.78	166	9	0.7	28	9	
	62	14	0.46	8.9	0.6	0.25	0.92	0.05	0.40	166	18	0.9	25	10	
morx	29	17	0.03	9.0	0.8	−0.51	*1.65*	*0.81*	*0.22*	*200*	*22*	*−0.5*	0	0	$N_V = 1$ (large f_V range)
	52	20	0.11	9.0	1.0	−0.68	*1.65*	*0.78*	*−0.14*	*200*	*21*	*−0.5*	*12*	*10*	
ptl	18	17	0.05	6.8	1.0	0.99	0.89	0.06	0.24	163	20	1.7	0	1	*IRAS* based
	23	17	0.20	6.8	0.8	0.78	0.89	0.05	0.07	163	21	1.3	0	1	
fixf	39	17	−0.30	9.0	–	–	0.98	–	–	214	–	–	27	11	fixed $R_\odot$, $V_\odot$, f_V
	44	20	−0.22	9.0	–	–	0.98	–	–	214	–	–	35	12	
	52	18	−0.14	9.0	–	–	0.98	–	–	214	–	–	38	11	
	67	19	0.08	9.0	–	–	0.98	–	–	214	–	–	34	9	
fix1	25	–	–	9.4	0.5	−0.04	0.95	0.05	−0.25	172	11	0.1	3	3	fixed ϕ (large f_V range)
fix2	45	–	–	9.3	0.7	0.18	0.98	0.05	−0.13	168	12	0.8	45	11	fixed ϕ (large f_V range)
fix3	65	–	–	9.8	0.4	−0.45	0.95	0.05	−0.51	173	12	0.1	12	6	fixed ϕ (large f_V range)

In runs **ptl** and **bdll**, $R_\odot$ is $\sim 2\sigma$ below the value of the other runs. The samples used in both runs have larger (apparent) scaleheights than the whole population of evolved stars; in **ptl** because the sample is incomplete in the plane and in **bdll** because the distribution of older stars simply has larger (intrinsic) scaleheight. Run **bdl**, however, the equivalent of **bdll** but without integration limit (see Section 3.1), results in an average value for $R_\odot$. Possibly, this can be explained by the fact that we are not using the integration limit and that the observed longitude range extends to $+10°$, i.e. the near tip of the bar is outside the window, as we mentioned before. This has a twofold effect. First, the surface-density asymmetry profile of the cut-off bar may look like the profile of an entire bar with larger viewing angle. We suggest that this is the origin of the ϕ values around 25°, as these are seen in **bdl, morx** and **ptl**. All samples that contain the **bdl** stars are clearly incomplete at larger distances to some extent, most of all **ptl** (the integration limit cannot be estimated for this sample). Apparently, the kinematics suppress the tendency for ϕ to be $\sim 25°$ (see also Fig. 6) if the incompleteness is not too strong, so that we only see it in run **morx**, which does not include kinematics, and in **bdl** and **ptl** with severe incompleteness (not taken into account). Secondly, one can imagine that with the far end of the bar 'cut off' in the data by the flux density limit and the near end cut off by the longitude limit, the result may look like a smaller bar, in other words larger $R_\odot$. This may cause the different $R_\odot$ in **bdl** and **bdll**. One would expect the larger $R_\odot$ in **ptl** if it did not have a longitude extending up to $+25°$.

Just as **bdll** and **ptl** have larger than average scaleheight, **bdh** has smaller scaleheight. Indeed, in **bdh** the value for $R_\odot$ is relatively large. The deviation is not as large as for **bdl**, as the **bdh** sample spans the whole bar and puts stringent constraints on the surface-density asymmetry profile.

The values for $V_\odot$ are rather low compared with the $200 \pm 20\,{\rm km\,s^{-1}}$ currently accepted (see Rohlfs et al. 1986; Feast & Whitelock 1997; Dehnen & Binney 1998). However, these determinations all assume $V_\odot$ is the local circular speed, which is unlikely, amongst other reasons because the disc may be slightly elliptical (Kuijken & Tremaine 1994). These authors advocate an average local circular velocity of $200\,{\rm km\,s^{-1}}$ and a tangential velocity for the LSR of $180\,{\rm km\,s^{-1}}$, making the low fitted values for $V_\odot$ more acceptable. The difference from the circular velocity of the model of $207\,{\rm km\,s^{-1}}$ is still large. In run **b**, $V_\odot$ is

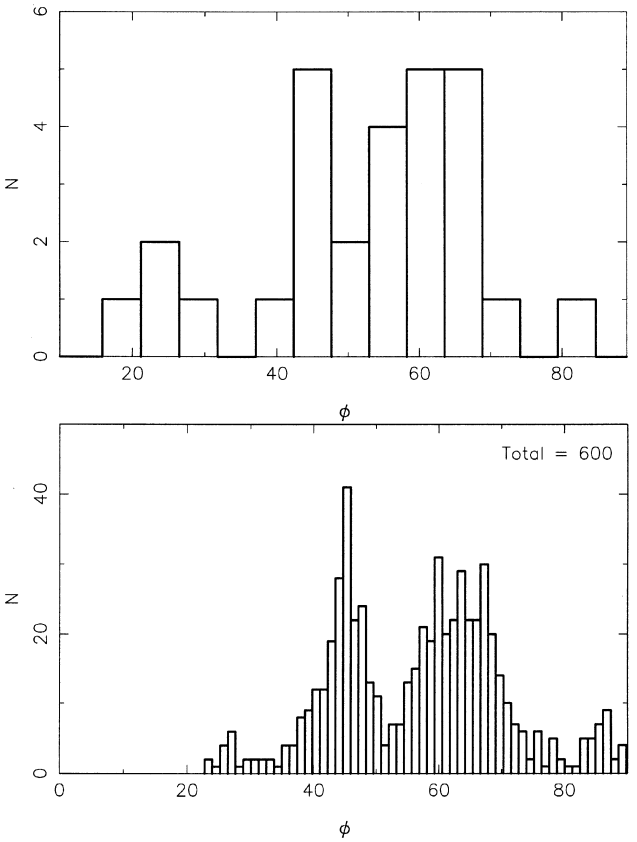

Figure 6. In the top panel, the histogram of all best-fitting values of ϕ (from Table 2) is shown; in the bottom panel the histogram of all 100 *W*-optimizing values from the six **bd*** runs. Note the narrow peak at 45°, the wide peak around 65° and the small peak around 25°, as well as the absence of values below 20°. The peak at 85° probably indicates near-symmetry (90°) of some data sets.

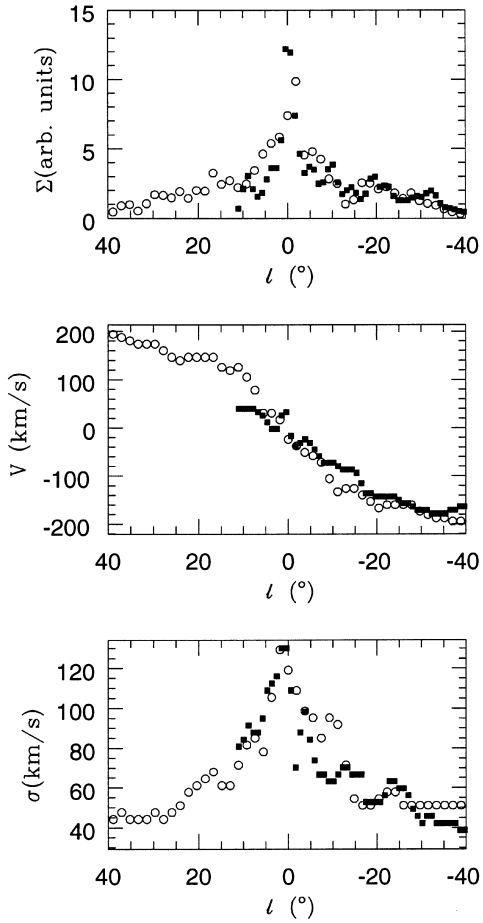

Figure 7. Surface density, mean galactocentric line-of-sight velocity and dispersion (all at $b = 0°$) for model **bd1** (open circles) and for data (total OH/IR sample) (filled squares). The points shown are obtained via three-dimensional adaptive-kernel smoothing. Note that hence the distributions are not reliable at the borders of the observed region ($\ell \gtrsim 7°; \ell \lesssim -42°$).

particularly ill-determined, because the sin ℓ term in the correction for the line-of-sight velocities (equation 1) covers a small range only.

Very high velocities (up to 450 km s^{-1}) are present in the initial *N*-body model that were never found for OH/IR stars. Altogether, fewer than 10 stars are known at absolute velocities higher than 300 km s^{-1} (Baud et al. 1975; van Langevelde et al. 1992; S97A). These high model velocities are not used in the comparison, however, because they are outside the windows defined in Table 1. Those windows are the true limits of the observations (S97A, S97B) so increasing the velocity window would be meaningless. The data–model comparison, in particular the determination of f_V, is therefore not based on the extreme tails, but on the wings of the distribution of the bulk of the velocities. The resulting $f_V < 1$ shows that the total mass M_p of the initial *N*-body model is somewhat too large.

4.2 Best model

As we have argued, the best values for the free parameters are given by the 44° solution of **bd**:**bd1**. From the free parameters we can derive some more interesting properties of the best-fitting model. The corotation radius is at 4.5 kpc and the semimajor axis of the bar is 2.5 kpc (cf. Section 3.1). The pattern speed is 46 km s^{-1} kpc^{-1} for the rescaled local circular velocity of 207 km s^{-1}. Finally, the mass of the bar is $1.7 \times 10^{10}\,M_\odot$. The plausibility of **bd1** is 15 ± 7 per cent, but when determining $\langle P \rangle$ with only the double-peaked stars (**bdd**), we obtain 68 ± 8 per cent. The single-peaked stars in **bd**, which possibly do not (all) belong to the OH/IR (asymptotic giant branch) star population, apparently decrease the goodness of the fit.

5 DISCUSSION

The value of 44° we obtain for ϕ is large compared with some other estimates [16°, Binney et al. 1991 (gas dynamics); 20°, Binney, Gerhard & Spergel 1997 (integrated light); 24°, Nikolaev & Weinberg 1997 (star counts); 20°–30°, Stanek et al. 1997 (flux differences between positive and negative longitudes)]. It should be noted that the lowest value for the viewing angle, 16° (Binney et al. 1991), is based on the possibly wrong assumption that the CO 'parallelogram' (Bally et al. 1988) is formed by gas on the inner cusped orbit (see Sevenster 1997). The parallelogram may well be the result of a tilt in the inner gas disc (Liszt & Burton 1978). Our high ϕ is compatible with the *COBE* E2 and E3 models ($\phi \sim 40°$) by Dwek et al. (1995) and with the value of 35° determined by Weiner & Sellwood (1996; from gas dynamics).

Also, Unavane & Gilmore (1998) find from near-infrared star counts that models with viewing angles between 20° and 45° are acceptable. A much older determination of ϕ from the gas dynamics also yields 45° (Peters 1975). To explain the two local star streams, Kalnajs (1997) argues that the viewing angle should be 45° as well.

Not only the high value for viewing angle, but also the value for the corotation radius, or pattern speed, can be reconciled with the observed gas kinematics. Various attempts to model H I and/or CO kinematics in the inner 4 kpc have given values for the pattern speed ranging from $\Omega_p \sim 19\,\mathrm{km\,s^{-1}\,kpc^{-1}}$ (Wada et al. 1996) to $63\,\mathrm{km\,s^{-1}\,kpc^{-1}}$ (Binney et al. 1991) or even $118\,\mathrm{km\,s^{-1}\,kpc^{-1}}$ (Yuan 1984). Hydrodynamic models for the H I longitude–velocity diagram of the whole Galaxy are illustrated in Mulder & Liem (1986), who themselves give as best model parameter $\phi = 20°$ and $R_{CR} \sim R_\odot$ (their fig. 5), but their model with $\phi = 40°$ and $R_{CR} \sim 0.5R_\odot$ (their fig. 9) gives a similarly good and arguably better fit to the 3-kpc arm and the central CO kinematics (Bally et al. 1988).

In Fig. 7, we illustrate how the data compare with the **bd1** model. The global agreement is good, and also the region around $\ell = -20°$, which may be in the corotation region of the Galaxy (Sevenster 1997), shows very similar features in all three quantities in model and data.

Fux himself (1997) derives a best-fitting value for ϕ of 25° with the same *N*-body model (his values for the other parameters are as in **fixf**, Table 2). We find that the values for ϕ found in run **fixf** are no different from the other runs. To mimic the model optimization from only the *COBE K*-band surface density (Fux 1997; his value f_V comes from scaling the velocities to fit the line-of-sight dispersion towards Baade's window) we introduced run **morx** where the kinematics are 'switched off' completely by setting $N_V = 1$. Indeed, one of the solutions gives $\phi = 29°$ (and $R_\odot = 9.0$ kpc), but it carries zero plausibility. As argued before, the global stellar kinematics seem essential in determining the viewing angle as they provide the necessary constraint to suppress the degenerating influence of limited windows and distance coverage. In Fux's (1997) case the longitude window (+30°, −30°) is large enough to prevent the problems we discussed in Section 4.1. However, latitudes $|\,b\,| < 3°$ are excluded from the optimization because the *COBE* data cannot be corrected reliably for extinction in the plane. This reminds us of run **ptl** with its incompleteness in the plane and subsequent low viewing angles and incapability of constraining the model ($\langle P \rangle = 0$ per cent). We would argue that many of the $\phi \sim 25° - 30°$ results found in the literature suffer from similar problems.

The measure for the relative residual defined by Fux, $R^2_{N_{pix}=300}$, is 1.5 per cent for **bd1** (cf. 0.47 per cent for his best fit for m08t3200).

It has proven virtually impossible to distinguish between triaxial and axisymmetric distributions by studying the distribution of the line-of-sight velocities only (e.g. Ibata & Gilmore 1995; Dejonghe et al. 1997). We applied the Kolmogorov–Smirnov test as used by Ibata & Gilmore (1995), as well as the intrinsically more powerful distance–velocity statistic described by Dejonghe et al. (1997), to the *N*-body model. Both only give significant results for very low latitudes ($|\,b\,| < 2°$) and even then only with samples of at least 1000 stars. The results are very dependent on the viewing angle. It is therefore no surprise that Ibata & Gilmore (1995) found no significant evidence for triaxiality from their intermediate-latitude velocity profiles and that neither statistic gives a signal when applied to the AOSP sample. However, even though the relatively low surface density of the AOSP sample inhibits the construction of velocity profiles, it contains sufficient kinematic evidence of triaxiality, as indicated by the plausibility of >50 per cent. The low latitudes, very homogeneous sampling and simultaneous fitting of the spatial and the kinematical distribution are essential.

In an earlier stage of this project, we applied the same procedure to the Schwarzschild-type *N*-body model of Zhao (1996) in its initial state before evolution. No significant fit was obtained for this unmixed model. Fux's *N*-body model has proven to have a solid physical basis and shows many observed features for a variety of data (Fux 1997; Fux & Friedli 1996). Also the formation of the *N*-body bar, spontaneously via instability of the underlying disc, is one of the probable ways of forming bars (e.g. Sellwood & Wilkinson 1993). The fact that for the **ptl** sample, selected especially for its incompleteness (see Section 3.2), no significant fits can be obtained, gives extra credibility to the model (as well as the method). This all provides proof that m08t3200, Fux's (1997) best model, gives a very good representation of the six-dimensional Galaxy.

Clearly, there is room for improvement, especially to lift the ϕ degeneracy once and for all. The most important features of a stellar data set used to achieve this are a large longitude range and homogeneous sampling of low latitudes. More dimensions to limit the degrees of freedom are preferred over more objects.

6 MICROLENSING OPTICAL DEPTH IN THE LINE OF SIGHT TO THE BAR

In this section, we want to discuss briefly the microlensing properties of the scaled model. The observed microlensing optical depth is as yet unaccounted for by any density model for the central Galaxy so it is important to assess this optical depth for our best model. In a forthcoming paper, we will do this in more detail and also calculate the event-duration distribution, which may give insight into the nature of the missing optical depth, even though the stellar mass function is not known in the model.

The microlensing optical depth τ is the probability of detecting a microlensing event at a given instant. From a density model, one can calculate the distribution of τ on the sky; the microlensing optical depth map. Comparison with the measured values [$\tau = 3.9^{+1.8}_{-1.2} \times 10^{-6}$ for red clump giants toward ($\ell = 2.^\circ 55$,

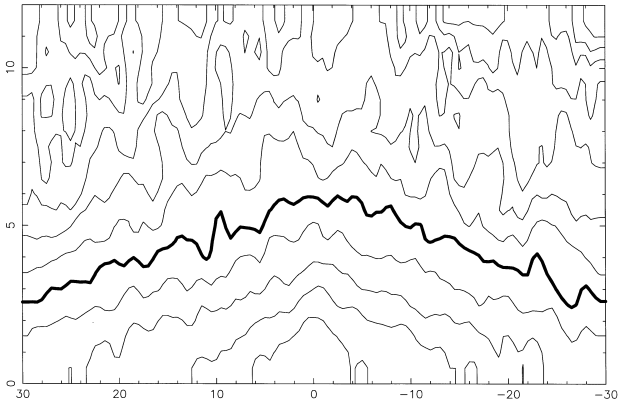

Figure 8. Microlensing optical depth (τ_0) map, symmetrized in latitude, for **bd1**, without the contribution of the dark particles in the simulation (see Fux 1997). The thick contour is for $\tau_0 = 1.0 \times 10^{-6}$; the other contours are spaced by a factor of 1.5, decreasing with increasing latitude.

$b = -3.^{\circ}64$); $\tau = 2.1^{+0.5}_{-0.4} \times 10^{-6}$ for main-sequence stars, corrected for blending, toward ($\ell = 2.^{\circ}7, b = -4.^{\circ}1$), Alcock et al. 1997; $\tau = 3.3^{+1.2}_{-1.2} \times 10^{-6}$toward Baade's window ($\ell \sim 1^{\circ}$, $b \sim -4^{\circ}$), Udalski et al. 1994] gives important information about the model. For a wide range of models that derive from the *COBE* maps (Dwek et al. 1995), one finds $\tau_{\rm mod}$ to be 2σ lower than $\tau_{\rm obs}$ (Zhao & Mao 1996). The missing optical depth thus has to be accounted for, within the limits put by other observations, by a component not present in those models; either dark or substellar particles or an extra density component (e.g. a thick disc).

For the calculation of τ one needs to take the brightness of the lensed sources into account. This is some function of their distance $D_{\rm s}$, so that the optical depth in a certain direction also depends on $D_{\rm s}$. Kiraga & Paczynski (1994) hence defined $\tau_\beta \propto D_s^{2+2\beta}$, where β defines the exact dependence on $D_{\rm s}$ and from the subscript of τ one can immediately see which dependence was used in the theoretical calculation. For $\beta = 0$, the sources are visible out to infinity; we obtain $\tau_0 \propto D_s^2$ and the proportionality is a straightforward volume correction.

For **bd1**, we calculated the τ_0 map (Fig. 8), as described in Fux (1997). It is well known that only a strong and massive bar, with a viewing angle smaller than 20° (Kiraga & Paczynski 1994; Zhao & Mao 1996; Fux 1997, his fig. 13; Zhao 1997a), can fully account for the measured values. Models derived from observed surface-density measurements have bars too weak, and mostly at too high viewing angles, to be able to account for τ (e.g. Nikolaev & Weinberg 1997). The values we obtain in the direction of the measurements are $\tau_0 \sim 1.5 \times 10^{-6}$, best compared with the 3.9×10^{-6} value for the clump giants, and $\tau_{-1} \sim 0.9 \times 10^{-6}$, best compared with 2.1×10^{-6}. Indeed both τ_0 and τ_{-1} (both without the contribution of the dark component) are too low by $>2\sigma$ to explain observations, thus confirming the preliminary results presented by Valls-Gabaud et al. (1997).

The distribution of the microlensing optical depth is not very bulge-like; it is dominated by lenses in the disc. There is no significant asymmetry between positive and negative longitudes, as would be expected when either lenses or sources (or both) have a barred distribution (see Evans 1994). However, the asymmetries in the optical depth distribution from disc lenses and bar lenses, respectively, have opposite signs (Evans 1994). Simple tests, with $\beta = 0, -1$, show that disc lenses skew the distribution toward positive longitudes; bar lenses toward negative longitudes. The net effect clearly depends on β, ϕ and density parameters.

In fact, the asymmetric signal is expected to be largest for a viewing angle of 45° (e.g. Evans 1994). In principle, since in Fig. 8 we show the τ_0 map ($\beta = 0$), we expect the distribution to be skewed toward negative longitudes. Additional spiral arms, protruding from the ends of the bar (see Fux 1997, m08t3200 model), could counteract this asymmetry. All in all, the symmetric appearance of Fig. 8 is understandable.

7 CONCLUSIONS

We presented values for the free parameters of a self-consistent model of the Galaxy, optimized to fit positions and velocities of various sets of evolved stars. These stars are representative for the global galactic distribution. The method is found to be sensitive to incompletenesses and to large-scale kinematics.

The overall distribution of the stars is fitted well by a bar with a global form like that of the *N*-body model (Fux 1997) with a semimajor axis of 2.5 kpc, corotation radius of 4.5 kpc, axis ratio of 0.5 and viewing angle of 44°. The value for the viewing angle is high but not incompatible with previous determinations from stellar data as well as gas kinematics. The mass contained within this bar is $\sim 1.7 \times 10^{10}\,{\rm M}_\odot$, marginally lower than various other derivations (Kent 1992; Blum 1995; Zhao, Rich & Spergel 1996). The derived pattern speed for the bar, $\Omega_{\rm p} = V_{\rm c}(R_{\rm CR})/R_{\rm CR}$, is $46\,{\rm km\,s^{-1}\,kpc^{-1}}$. For the solar azimuthal velocity a low value of $171\,{\rm km\,s^{-1}}$ is found. This is much lower than the local circular velocity ($207\,{\rm km\,s^{-1}}$) in the model potential, implying that the Sun (more precisely, the local standard of rest) would not be on a circular orbit in this particular model. This is in agreement with the findings of Kuijken & Tremaine (1994) who find a local circular velocity of $200\,{\rm km\,s^{-1}}$ and $V_\odot = 180\,{\rm km\,s^{-1}}$.

We argue that using low-latitude, unbiased, global stellar kinematics is crucial to determine the viewing angle ϕ. The commonly found and accepted low value of $\phi \sim 25^{\circ}$ (see Section 5) should be viewed with caution. Our method, applied to a variety of data sets with 'known flaws' or to the stellar positions only, shows that indeed these data sets favour viewing angles around the lower value. The resulting fits do not have high plausibility.

One of the reasons is that the signal of the bar diminishes quickly with increasing latitude and thus ϕ becomes ill-constrained. The sample of **ptl**, which under-represents the plane below $\sim 3^{\circ}$ – approximately one scaleheight – gives a null result. This means that either there has not been significant bar-induced thickening in the inner Galaxy, or the thickening conspires with the distribution, becoming rounder. We believe that parameters of the Galactic bar cannot be reliably constrained without data that trace its innermost 1 scaleheight.

This also means that Baade's window may not be an appropriate region in which to sample bar properties (see also Sevenster 1997). Regardless of this consideration, with the best-model viewing angle of 45° the bar does not give significantly higher values for τ than do a variety of axisymmetric distributions (Kuijken 1997; Zhao 1997a) and $\tau_{\rm mod} \sim 0.5\tau_{\rm obs}$ for our best model. We conclude that (provided that the value of $\tau_{\rm obs}$ is beyond suspicion) the origin of the discrepancy between current bar models and the observed microlensing optical depth should be sought in a foreground component – e.g. a spiral arm or a thick disc – with larger apparent scaleheight than the bar. The most convincing argument in favour of a small viewing angle for the bar (Zhao 1997a) is thus taken away.

ACKNOWLEDGMENTS

MNS thanks Mt Stromlo and Siding Spring Observatories for hospitality during the start of this project. The visit was financed from an Amelia Earhart Fellowship granted by Zonta International Foundation. DVG also thanks MSSSO for their warm hospitality, and the French–Australian Committee for Astronomy for travel support. Useful suggestions and hints by Tim de Zeeuw, Adriaan Blaauw and the referee David Spergel are acknowledged.

REFERENCES

Alcock C. et al., 1997, ApJ, 479, 119
Bally J., Stark A., Wilson R., Henkel C., 1988, ApJ, 324, 223
Baud B., Habing H., Matthews H., O'Sullivan J., Winnberg A., 1975, Nat, 258, 406

Binney J. J., Gerhard O. E., Stark A. A., Bally J., Uchida K. I., 1991, MNRAS, 252, 210
Binney J. J., Gerhard O. E., Spergel D. N., 1997, MNRAS, 288, 365
Blum R., 1995, ApJ, 444, L89
Charbonneau P., 1995, ApJS, 101, 309
Dehnen W., Binney J., 1998, MNRAS, 294, 429
Dejonghe H., Vauterin P., Caelenberg van K., Durand S., Mathieu A., 1997, in Habing H., Lamers H., eds, IAU Symp. 180, Planetary Nebulae, Kluwer, Dordrecht, p. 428
Dwek E. et al., 1995, ApJ, 445, 716
Elmegreen B., 1996, in Buta R., Crocker D., Elmegreen B., eds, PASP Conf. Ser. Vol. 91, Barred Galaxies, p. 197
Evans N. W., 1994, ApJ, 437, L31
Feast M., Whitelock P., 1997, MNRAS, 291, 683
Frogel J., 1988, ARA&A, 26, 51
Fux R., 1997, A&A, 327, 983
Fux R., Friedli D.., 1996, in Buta R., Crocker D., Elmegreen B., eds, PASP Conf. Ser. Vol. 91, Barred Galaxies, p. 529
Gerhard O., 1996, in Blitz L., Teuben P., eds, Proc. IAU Symp. 169, Unsolved problems of the Milky Way. Reidel, Dordrecht, p. 79
Habing H. J., 1993, in Dejonghe H., Habing H. J., eds, Proc. IAU Symp. 153, Galactic Bulges. Reidel, Dordrecht, p. 57
Ibata R., Gilmore G., 1995, MNRAS, 275, 605
Kalnajs A. J., 1997, in Sandqvist A., Lindblad P., eds, Lecture Notes in Physics 474, Barred Galaxies and Circumstellar Activity, Springer-Verlag, Heidelberg, p. 165
Kent S., 1992, ApJ, 387, 181
Kiraga M., Paczynski B., 1994, ApJ, 430, L101
Kuijken K., 1997, ApJ, 486, L19
Kuijken K., Tremaine S., 1994, ApJ, 421, 178
Liszt H., Burton W., 1978, ApJ, 226, 790
Mulder W., Liem B., 1986, A&A, 157, 148
Nikolaev S., Weinberg M., 1997, ApJ, 487, 885
Noguchi M., 1996, in Buta R., Crocker D., Elmegreen B., eds, PASP Conf. Ser. Vol. 91, Barred Galaxies, Astron. Soc. Pac., San Francisco, p. 339
Peters W., 1975, ApJ, 195, 617
Press W., Teukolsky S., Vetterling W., Flannery B., 1992, Numerical Recipes, Cambridge Univ. Press, Cambridge
Rohlfs K., Boehme R., Chini R., Wink J., 1986, A&A, 158, 181
Saha P., 1998, AJ, 115, 1206
Schwarzschild M., 1979, ApJ, 232, 236
Sellwood J., Wilkinson A., 1993, Rep. Prog. Phys., 56, 173
Sevenster M. N., 1997, PhD dissertation, Leiden Univ.
Sevenster M. N., Chapman J. M., Habing H. J., Killeen N. E. B., Lindqvist M., 1997a, A&AS, 122, 79 (S97A)
Sevenster M. N., Chapman J. M., Habing H. J., Killeen N. E. B., Lindqvist M., 1997b, A&AS, 124, 509 (S97B)
Stanek K., Udalski A., Szymanski M., Kaluzny J., Kubiak M., Mateo M., Krzeminski W., 1997, ApJ, 477, 163
te Lintel Hekkert P., Caswell J., Habing H. J., Haynes R., Wiertz W., 1991, A&AS, 90, 327
Udalski A. et al., 1994, Acta Astron., 44, 165
Unavane M., Gilmore G., 1998, MNRAS, 295, 145
Valls-Gabaud D., Saha P., Sevenster M., Fux R., 1997, in Ferlet R., Maillard J., Raban B., eds, Variable stars and astrophysical returns of microlensing surveys. Editions Frontières, Gif-sur-Yvette, p. 119
van der Veen W., 1989, A&A, 210, 127
van Langevelde H., Brown A., Lindvist M., Habing H., de Zeeuw P., 1992, A&A, 261, L17
Wada K., Taniguchi Y., Habe A., Hasegawa T., 1996, in Buta R., Crocker D., Elmegreen B., eds, PASP Conf. Ser. Vol. 91, Barred Galaxies, p. 554
Weiner B., Sellwood J., 1996, in Blitz L., Teuben P., eds, Proc. IAU Symp. 169, Unsolved problems of the Milky Way. Reidel, Dordrecht, p. 145
Yuan C., 1984, ApJ, 281, 600
Zhao H. S., 1996, MNRAS, 283, 149
Zhao H. S., 1997a, in Ferlet R., Maillard J., Raban B., eds, Variable stars and astrophysical returns of microlensing surveys. Editions Frontières, Gif-sur-Yvette, p. 109
Zhao H. S., 1997b, preprint (astro-ph 9705046)
Zhao H. S., Mao S., 1996, MNRAS, 283, 1197
Zhao H. S., Rich R. M., Spergel D., 1996, MNRAS, 282, 175

This paper has been typeset from a TEX/LATEX file prepared by the author.